This paper is published as part of a PCCP Themed Issue on:

Physical chemistry of solids – the science behind materials engineering

Guest Editors: Jürgen Janek, Manfred Martin and Klaus Dieter Becker

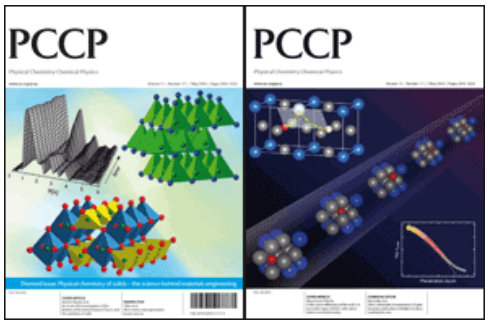

Editorial

Physical chemistry of solids—the science behind materials engineering
Phys. Chem. Chem. Phys., 2009
DOI: 10.1039/b905911n

Perspectives

Nanoionics: ionic charge carriers in small systems
Joachim Maier, *Phys. Chem. Chem. Phys.*, 2009
DOI: 10.1039/b902586n

Micro-ionics: next generation power sources
Harry L. Tuller, Scott J. Litzelman and WooChul Jung, *Phys. Chem. Chem. Phys.*, 2009
DOI: 10.1039/b901906e

Communications

On the conduction pathway for protons in nanocrystalline yttria-stabilized zirconia
Sangtae Kim, Hugo J. Avila-Paredes, Shizhong Wang, Chien-Ting Chen, Roger A. De Souza, Manfred Martin and Zuhair A. Munir, *Phys. Chem. Chem. Phys.*, 2009
DOI: 10.1039/b901623f

Direct calorimetric measurement of grain boundary and surface enthalpies in yttria-stabilized zirconia
Shushu Chen, Hugo J. Avila-Paredes, Sangtae Kim, Jinfeng Zhao, Zuhair A. Munir and Alexandra Navrotsky, *Phys. Chem. Chem. Phys.*, 2009
DOI: 10.1039/b819740g

Papers

Elastic strain at interfaces and its influence on ionic conductivity in nanoscaled solid electrolyte thin films—theoretical considerations and experimental studies
N. Schichtel, C. Korte, D. Hesse and J. Janek, *Phys. Chem. Chem. Phys.*, 2009
DOI: 10.1039/b900148d

Chemical and electronic properties of the ITO/Al_2O_3 interface
Yvonne Gassenbauer, André Wachau and Andreas Klein, *Phys. Chem. Chem. Phys.*, 2009
DOI: 10.1039/b822848e

Electronic state of oxygen nonstoichiometric $La_{2-x}Sr_xNiO_{4+\delta}$ at high temperatures
Takashi Nakamura, Keiji Yashiro, Kazuhisa Sato and Junichiro Mizusaki, *Phys. Chem. Chem. Phys.*, 2009
DOI: 10.1039/b823364k

B-Site cation diffusivity of Mn and Cr in perovskite-type $LaMnO_3$ with cation-deficit nonstoichiometry
Shogo Miyoshi and Manfred Martin, *Phys. Chem. Chem. Phys.*, 2009
DOI: 10.1039/b901208g

High anion conductivity in a ternary non-equilibrium phase of BaF_2 and CaF_2 with mixed cations
B. Ruprecht, M. Wilkening, A. Feldhoff, S. Steuernagel and P. Heitjans, *Phys. Chem. Chem. Phys.*, 2009
DOI: 10.1039/b901293a

Electrical and optical characterization of undoped $BaTiO_3$ in the quenched state
K.-D. Becker, M. Schrader, H.-S. Kwon and H.-I. Yoo, *Phys. Chem. Chem. Phys.*, 2009
DOI: 10.1039/b823174e

Oxidation states of Co and Fe in $Ba_{1-x}Sr_xCo_{1-y}Fe_yO_{3-\delta}$ (x, y = 0.2–0.8) and oxygen desorption in the temperature range 300–1273 K
Ashley S. Harvey, F. Jochen Litterst, Zhen Yang, Jennifer L. M. Rupp, Anna Infortuna and Ludwig J. Gauckler, *Phys. Chem. Chem. Phys.*, 2009
DOI: 10.1039/b819414a

Bulk defect chemistry and surface electronic behavior of Zn,Sn codoped In_2O_3 transparent conducting oxides
Steven P. Harvey, Thomas O. Mason, Christoph Körber and Andreas Klein, *Phys. Chem. Chem. Phys.*, 2009
DOI: 10.1039/b822149a

Defect chemistry of the cage compound, $Ca_{12}Al_{14}O_{33-\delta}$—understanding the route from a solid electrolyte to a semiconductor and electride
Doh-Kwon Lee, Lutz Kogel, Stefan G. Ebbinghaus, Ilia Valov, Hans-Dieter Wiemhoefer, Martin Lerch and Juergen Janek, *Phys. Chem. Chem. Phys.*, 2009
DOI: 10.1039/b818474g

Electrical conductivity–defect structure correlation of variable-valence and fixed-valence acceptor-doped $BaTiO_3$ in quenched state
Han-Ill Yoo, Tae-Sik Oh, Hyung-Soon Kwon, Dong-Kyu Shin and Jong-Sook Lee, *Phys. Chem. Chem. Phys.*, 2009
DOI: 10.1039/b822381p

An *in situ* XAS investigation of the kinetics of the ammonolysis of Ga_2O_3 and the oxidation of GaN
J. Brendt, D. Samuelis, T. E. Weirich and M. Martin, *Phys. Chem. Chem. Phys.*, 2009
DOI: 10.1039/b901819k

***In situ* investigation of coloration processes in $LiNbO_3$: MgO during reducing/oxidizing high-temperature treatments**
Dmytro Sugak, Yaroslav Zhydachevskii, Yuriy Sugak, Oleg Buryy, Sergii Ubizskii, Ivan Solskii, Alexander Börger and Klaus-Dieter Becker, *Phys. Chem. Chem. Phys.*, 2009
DOI: 10.1039/b822631h

Voltage-assisted ^{18}O tracer incorporation into oxides for obtaining shallow diffusion profiles and for measuring ionic transference numbers: basic considerations
J. Fleig, *Phys. Chem. Chem. Phys.*, 2009
DOI: 10.1039/b822415c

Oxygen incorporation into strontium titanate single crystals from CO_2 dissociation
Chr. Argirusis, F. Voigts, P. Datta, J. Grosse-Brauckmann and W. Maus-Friedrichs, *Phys. Chem. Chem. Phys.*, 2009
DOI: 10.1039/b901401b

Nearly constant loss effects in borate glasses
David M. Laughman, Radha D. Banhatti and Klaus Funke, *Phys. Chem. Chem. Phys.*, 2009
DOI: 10.1039/b822561n**Switching behaviour of modulated ferroelectrics I: kinetics of the field-induced lock-in transition of Rb_2ZnCl_4**
K. Elisbihani, H. Gibhardt and G. Eckold, *Phys. Chem. Chem. Phys.*, 2009
DOI: 10.1039/b902368b

Construction of nano- and microporous frameworks from octahedral bubble clusters
S. M. Woodley, M. B. Watkins, A. A. Sokol, S. A. Shevlin and C. R. A. Catlow, *Phys. Chem. Chem. Phys.*, 2009
DOI: 10.1039/b902600b

Bubbles and microporous frameworks of silicon carbide
M. B. Watkins, S. A. Shevlin, A. A. Sokol, B. Slater, C. R. A. Catlow and S. M. Woodley, *Phys. Chem. Chem. Phys.*, 2009
DOI: 10.1039/b902603g

Band gap engineering of ZnO *via* doping with manganese: effect of Mn clustering
Hilkka Saal, Thomas Bredow and Michael Binnewies, *Phys. Chem. Chem. Phys.*, 2009
DOI: 10.1039/b901596e

Transport pathways for mobile ions in disordered solids from the analysis of energy-scaled bond-valence mismatch landscapes
Stefan Adams and R. Prasada Rao, *Phys. Chem. Chem. Phys.*, 2009
DOI: 10.1039/b901753d

Ultrathin oxide films and heterojunctions: CaO layers on BaO and SrO
Chris E. Mohn, Neil L. Allan and John H. Harding, *Phys. Chem. Chem. Phys.*, 2009
DOI: 10.1039/b822588e

Formation entropies of intrinsic point defects in cubic In_2O_3 from first-principles density functional theory calculations
Péter Ágoston and Karsten Albe, *Phys. Chem. Chem. Phys.*, 2009
DOI: 10.1039/b900280d

Hydrogen adsorption on Pd-containing Au(111) bimetallic surfaces
Sudha Venkatachalam and Timo Jacob, *Phys. Chem. Chem. Phys.*, 2009
DOI: 10.1039/b900250b

Interdiffusion and surface-sandwich ordering in initial Ni-core–Pd-shell nanoparticle
Alexander V. Evteev, Elena V. Levchenko, Irina V. Belova and Graeme E. Murch, *Phys. Chem. Chem. Phys.*, 2009
DOI: 10.1039/b822112j

First-principles study on defect chemistry and migration of oxide ions in ceria doped with rare-earth cations
Masanobu Nakayama and Manfred Martin, *Phys. Chem. Chem. Phys.*, 2009
DOI: 10.1039/b900162j**An electrochemical study of lithium insertion into $Cr_{5-y}Ti_ySe_8$ (y = 1, 2, 3, 4, 4.5) beyond the intercalation limit**
Sylvio Indris, Joseph Wontcheu and Wolfgang Bensch, *Phys. Chem. Chem. Phys.*, 2009
DOI: 10.1039/b822397a

Mixed $LiCo_{0.6}M_{0.4}PO_4$ (M = Mn, Fe, Ni) phosphates: cycling mechanism and thermal stability
Natalia N. Bramnik, Dmytro M. Trots, Heiko J. Hofmann and Helmut Ehrenberg, *Phys. Chem. Chem. Phys.*, 2009
DOI: 10.1039/b901319a

Changes in the crystal and electronic structure of $LiCoO_2$ and $LiNiO_2$ upon Li intercalation and de-intercalation
Sonja Laubach, Stefan Laubach, Peter C. Schmidt, David Ensling, Stefan Schmid, Wolfram Jaegermann, Andreas Thißen, Kristian Nikolowski and Helmut Ehrenberg, *Phys. Chem. Chem. Phys.*, 2009
DOI: 10.1039/b901200a

Partial oxidation of methanol on well-ordered V_2O_5(001)/Au(111) thin films
J. M. Sturm, D. Göbke, H. Kuhlenbeck, J. Döbler, U. Reinhardt, M. V. Ganduglia-Pirovano, J. Sauer and H.-J. Freund, *Phys. Chem. Chem. Phys.*, 2009
DOI: 10.1039/b822384j

Investigation of the nucleation and growth dynamics of FePt nanoparticles prepared *via* a high-temperature synthesis route employing $PtCl_2$ as platinum precursor
Hauke Heller, Kirsten Ahrenstorf, Jose A. C. Broekaert and Horst Weller, *Phys. Chem. Chem. Phys.*, 2009
DOI: 10.1039/b822306h

Non-oxidic nanoscale composites: single-crystalline titanium carbide nanocubes in hierarchical porous carbon monoliths
Kirstin Sonnenburg, Bernd M. Smarsly and Torsten Brezesinski, *Phys. Chem. Chem. Phys.*, 2009
DOI: 10.1039/b822437d

Poly(p-phenylene sulfone)s with high ion exchange capacity: ionomers with unique microstructural and transport features
C. C. de Araujo, K. D. Kreuer, M. Schuster, G. Portale, H. Mendil-Jakani, G. Gebel and J. Maier, *Phys. Chem. Chem. Phys.*, 2009
DOI: 10.1039/b822069g

Pulsed electrodeposition of porous ZnO on Ag-coated polyamide filaments
Melanie Rudolph, Thomas Loewenstein, Elisa Arndt, Yvonne Zimmermann, Andreas Neudeck and Derck Schlettwein, *Phys. Chem. Chem. Phys.*, 2009
DOI: 10.1039/b822534f

First-principles study on defect chemistry and migration of oxide ions in ceria doped with rare-earth cations

Masanobu Nakayama*[ab] and Manfred Martin[b]

Received 7th January 2009, Accepted 11th February 2009
First published as an Advance Article on the web 11th March 2009
DOI: 10.1039/b900162j

Oxygen transport in rare-earth oxide (RE_2O_3) doped CeO_2 with fluorite structure has attracted considerable attention owing to both the range of practical usage (*e.g.*, fuel cells, sensors, *etc.*) and the fundamental fascination of fast oxide ion transport in crystalline solids. Using density-functional theory, we have calculated the formation energies of point defects and their migration properties in RE_2O_3 doped CeO_2 (RE = Sc, Y, La, Nd, Sm, Gd, Dy, and Lu). The calculated results show that oxygen vacancies are the dominant defect species obtained by RE^{3+} doping. They form associates with the RE^{3+} ions, and the corresponding defect association energy is a strong function of the ionic radii of the RE^{3+} dopants. The migration of an oxygen vacancy was investigated using the nudged elastic band method. The lowest activation energy for oxygen vacancy hopping is obtained for a straightforward migration path between two adjacent oxygen sites. The migration energy of an oxygen vacancy also strongly depends on the ionic radii of the neighbouring dopant cations. Accordingly, we have identified two factors that affect the oxygen vacancy migration; (1) trapping (or repelling) of an oxygen vacancy at the NN site of the RE^{3+} dopant, and (2) reduction (or enlargement) of the migration barrier by RE^{3+} doping. These findings provide insight for atomistic level understanding of ionic conductivity in doped ceria and would be beneficial for optimizing ionic conductivity.

1. Introduction

Oxide ion transport in ceria (CeO_2) based materials with a fluorite structure is of great interest in the development of electrolytes for solid oxide fuel cells due to its high ionic conductivity.[1,2] Pure CeO_2 itself is not a good ionic conductor, but a significant increase in conductivity can be achieved by rare-earth oxide (RE_2O_3: RE denotes a rare-earth element) doping due to creation of oxygen vacancies. Therefore, RE_2O_3 doped CeO_2 materials have been studied extensively for many years by measuring the oxide ion conductivities and their activation energies as functions of the dopant concentration and/or the temperature.[3,4] The results showed a strong dependence of the conductivity on the ionic radius of the dopants. The maximum conductivity was observed in CeO_2 doped with Sm_2O_3 while replacement of Ce^{4+} by larger or smaller RE^{3+} ions than Sm^{3+} caused a decrease in ionic conduction.[4] The effect is believed to be due to the local structure driven properties, such as local distortion or lattice strain owing to the size mismatch between host Ce^{4+} ions and dopant RE^{3+} ions, and the trapping effect of the oxygen vacancies by the dopant ions. For example, Gerhardt-Anderson *et al.* suggested that trapping effects stem from the formation of a (RE_{Ce}' $V_O^{\bullet\bullet}$) cluster on nearest neighbour (NN) or on next nearest-neighbor (NNN) positions.[3] Based on this idea, they estimated the defect association enthalpies from conductivity measurements. Smaller size ions (*e.g.* Sc^{3+}) among the series of RE dopants resulted in strong association, and *vice versa*. These results are qualitatively reproduced by computations using a Born-like empirical potential model.[5] Similarly, Zacate *et al.* reported for doped ZrO_2 (fluorite structure) that the defect association enthalpy (or binding energy) between a dopant RE^{3+} ion and a nearest neighbour (NN) oxygen vacancy decreases with decrease of the ionic radius of the RE^{3+} ions.[6] Very recently, Wei *et al.* calculated the defect association energy in CeO_2 doped with 9 types of rare-earth oxides using also an empirical potential model.[7] A clear tendency was found that small dopants attract an oxygen vacancy, while strong association occurs between Ce^{4+} and an oxygen vacancy for large dopants. An EXAFS study of RE_2O_3 doped CeO_2 reported by Yoshida *et al.* confirmed that oxygen vacancies tend to be associated with RE^{3+} dopants.[8] On the other hand, molecular-dynamics (MD) simulations using empirical potentials in yttria-stabilized ZrO_2 revealed that the difference in conductivity at different dopant concentrations is not caused by defect association between oxygen vacancies and the Y^{3+} dopant but rather due to the strongly reduced hopping probabilities of oxygen ions around Y^{3+} dopant ions.[9] However, the computational approaches using Born-like potential model in the above studies[5–7,9] may suffer from the precise assignments of potential parameters due to the increase of the number of parameters with increasing number of dopant species. In this respect, the first-principles DFT approach is advantageous due to the absence of adjustable (empirical) parameters in its formalism. Yoshida *et al.* studied the migration energy of Y, La and Sm doped ceria[10] and suggested a relationship between the ionic

[a] *Department of Applied Chemistry, Tokyo Institute of Technology, Ookayama, Meguro-ku, Tokyo, 152-8552, Japan*
[b] *Institute of Physical Chemistry, RWTH Aachen University, Landoltweg 2, 52056 Aachen, Germany. Fax: +81 3 5734 2146; Tel: 81 3 5734 2145*

conductivity and the lattice deformation. Andersson *et al.* reported recently a first-principles DFT study on dopant-oxygen vacancy interaction, or the defect association energy and the migration barrier, in CeO_2 doped with various rare earth oxides.[11] They showed a clear relationship between the defect interactions and the atomic number (or ionic radius) of the RE dopant, and they predicted an effective activation energy for ionic conduction. However, the computational results in[10,11] were derived from a few specific RE/Ce/O/vacancy configurations.

Therefore, a comprehensive understanding of the energetics concerning (1) the defect chemistry and (2) the migration of oxygen vacancies is required to clarify the effect of different RE^{3+} dopants and different local configurations on oxygen transport in RE_2O_3 doped CeO_2. In this paper, first-principles density functional theory (DFT) is adopted to reveal the influence of the above two factors in CeO_2 doped with eight different RE_2O_3. As rare earth element Sc, Y, La, Nd, Sm, Gd, Dy, and Lu were chosen to cover a wide range of ionic radii from $\sim$1.0 to $\sim$1.3 Å. In addition, several atomic configurations were considered to understand comprehensively the effects of local atomic arrangements for defect association and migration barriers.

The first-principles DFT approach will give us an atomistic level understanding of the macroscopic oxide ion transport phenomena, and this insight could be used for the design of materials with improved properties. For example, Murray *et al.* simulated the oxide ion conductivity in Y_2O_3 doped CeO_2 by combining atomistic simulation methods and Monte Carlo simulations.[12] Krishnamurthy *et al.*[13,14] and Pomprasertsuk *et al.*[15] reported combined first-principles DFT and Monte Carlo techniques for Y_2O_3 doped ZrO_2. Thus, the aim of this paper is to gain knowledge of the energies related to defect chemistry and migration barriers which is the first step on the way to predict the ionic conductivity. In the following steps these energies must be expanded and linked to the macroscopic behaviour and properties. For example, these energies could be used directly in the above models[12–15] to predict the macroscopic ionic conductivity. In this respect, we will use the present computational results along with a simplified conductivity model proposed in ref. 16 to demonstrate qualitatively the dependence of the ionic conduction behaviour on the dopant fraction in Y_2O_3 doped Ceria.

This paper is arranged as follows. Section 1 contains the introduction. Section 2 describes the details of the first-principles DFT procedure. Section 3 consists of two subsections that discuss the physical properties of pure CeO_2 (Sec. 3.1), and the defect chemistry of RE_2O_3 doped CeO_2 (Sec. 3.2). Section 4 contains the results of oxide ion migration (or oxide ion jumps between lattice sites) in pure ceria and in RE_2O_3 doped CeO_2. Finally, section 5 gives a summary and conclusions.

2. Computational methods

All first-principles DFT calculations were performed using the Vienna *ab initio* simulation package (VASP)[17,18] with the generalized gradient approximation (PBE-GGA)[19] and the projector-augmented wave (PAW) method.[20] (Recently, the importance for describing localized 4f states was pointed out, such as by using the so called DFT + U method.[21–27] However, this method was not used in this study, because the major ions of Ce^{4+} and O^{2-} in RE_2O_3 doped CeO_2 do not possess 4f electrons, and several adjustable U parameters for the different RE^{3+} ions would be needed which causes similar problems as the Born-like potential model mentioned before.) Spin polarization calculation was adopted. At first, we calculated 'perfect CeO_2' without any defects in the lattice, under the condition of full structural relaxation (*i.e.* allowing for the change of the cubic lattice parameter and the internal atomic positions). Then, the final energies of the optimized geometries were recalculated so as to correct for changes in the plane-wave basis during relaxation.

After determining the lattice parameter of pure CeO_2, we expanded the simulation cell to a size of $2 \times 2 \times 2$ conventional fluorite unit cells ($Ce_{32}O_{64}$) to model point defects, such as an oxygen vacancy, a substitutional cation, and their associates, but also the migration of oxygen ions. In all the computations, we controlled the total number of electrons in the lattice to compensate for excess charges of impurities or defects. For instance, when we assume the situation that an impurity RE atom replaces a Ce atom (*i.e.*, $[RECe_{31}O_{64}]^-$), one excess electron is added into the lattice. A jellium background was used to neutralize the lattice with charged point defects (oxygen vacancy and/or trivalent cations). It was also assumed that structural relaxation only affects the local surrounding of the defects in the $2 \times 2 \times 2$ superstructure. Thus, only internal atomic positions in the cell were allowed to relax and the cubic lattice parameter was fixed for the calculations. The validity of this approach was confirmed by the fact that the energy difference of oxygen vacancy formation was less than 0.01 eV for the two simulation cells $Ce_{32}O_{63}$ and $Ce_{48}O_{95}$.

The nudged elastic band (NEB) method was used to investigate the minimum energy pathways of the oxygen vacancy hopping from one lattice position to adjacent sites. First, the two point configurations (initial and end point) and the corresponding total energies were calculated by specifying the location of a vacancy at the two potential minima. In this computation, the internal atomic positions in the cell were relaxed without changing the lattice parameter, as mentioned above. Then intermediate configurations were generated by linear interpolation between the initial and end points. Finally, the intermediate configurations were relaxed under the constraint that the ions were connected by springs to keep the ions equidistant from neighbouring configurations during the relaxation. Details of the NEB method are described in ref. 28.

3. Results: defect chemistry

3.1 Perfect CeO_2

Table 1 lists the obtained cubic lattice parameter and the bulk modulus for perfect CeO_2 as obtained by DFT computations and by experiments. The conventional fluorite structure was calculated with a Ce_4O_8 superstructure using $5 \times 5 \times 5$ k-point meshes, and the bulk modulus was obtained along with Murnaghan's formula.[29] The present results show good agreement with previous studies within the typical

Table 1 Cubic lattice parameter and bulk modulus of CeO_2 obtained by density functional theory (DFT) computations and experiments

Property	Computation (DFT)	Experiments
Cubic lattice parameter/Å	5.463,[a] 5.45, [30] 5.37, [31] 5.48, [32] 5.45 [33]	5.41 [34]
Bulk modulus/GPa	181.03,[a] 193.5, [31] 187.7 [32]	236, [35] 204 [36]

[a] Present work.

DFT-GGA error. For later calculations of the defect structure and the migration of an oxygen vacancy, we used a $Ce_{32}O_{64}$-based superstructure as mentioned in the previous section. Thus, we compared the computational results for perfect CeO_2 using two different cell sizes, Ce_4O_8 and $Ce_{32}O_{64}$. For $Ce_{32}O_{64}$, numerical integration over the Brillouin zone was carried out only by sampling the Γ point due to limitations of our computational resources. The obtained total energy difference between Ce_4O_8 and $Ce_{32}O_{64}$ is small enough (1.1 meV per CeO_2) to ensure that our superstructure computations capture the physical and chemical properties with the quality presented in Table 1.

3.2 RE_2O_3 doped CeO_2

As pointed out in many reports, oxygen vacancy formation is mandatory for oxygen ion migration in ceria (or in fluorite structured oxides in general). One important intrinsic defect formation reaction is the Schottky reaction (eqn (2.1), Kröger–Vink notation)

$$\mathrm{nul} \leftrightarrow V_{Ce}^{////} + 2V_O^{\bullet\bullet} \quad (2.1)$$

Another candidate for oxygen vacancy creation is the Anti-Frenkel reaction (eqn (2.2))

$$O_o^{\,x} \leftrightarrow O_i^{//} + V_O^{\bullet\bullet} \quad (2.2)$$

Here, we assume the interstitial sites for oxygen ($O_i^{//}$) to be the 4b Wyckoff positions of the space group $Fm\bar{3}m$, or the large cavities at the centre of the fluorite structure. To calculate the defect formation energy for both reactions, we consider dilute conditions where the created point defects do not interact with each other. Thus, we can calculate the total energy $E_{tot}(N_{Ce},N_O)$ of a system that contains a single point defect in the supercell $Ce_{32}O_{64}$ separately, and then we can sum up the terms to obtain the reactions in the above eqns (2.1) and (2.2). The corresponding defect formation energies $E_{def}^{\,S}$ (Schottky defect) and $E_{def}^{\,AF}$ (Anti-Frenkel defect) are:

$$E_{def}^{\,S} = E_{tot}([Ce_{31}V_{Ce}\,O_{64}]^{4-}) + 2\,E_{tot}([Ce_{32}O_{63}V_O]^{2+}) - 95\,E_{tot}([CeO_2]) \quad (2.3)$$

$$E_{def}^{\,AF} = E_{tot}([Ce_{32}O_{64}O_i]^{2-}) + E_{tot}([Ce_{32}O_{63}V_O]^{2+}) - 64\,E_{tot}([CeO_2]) \quad (2.4)$$

Here V_{Ce}, V_O and O_i indicate a cerium vacancy, an oxygen vacancy and an oxygen interstitial ion, respectively. The results are shown in the Table 2. For comparison, the Frenkel reaction

$$Ce_{Ce}^{\,x} \leftrightarrow Ce_i^{\bullet\bullet\bullet\bullet} + V_{Ce}^{////} \quad (2.5)$$

Table 2 Defect formation energies of intrinsic defects and fractions at 1000 K in pure ceria

Defect formation reaction	Law of mass action and calculated defect formation energy	Fraction of defects in CeO_2 at 1000 K
Schottky (eqn (2.1))	$K_S = [V_{Ce}^{////}]\cdot[V_O^{\bullet\bullet}]^2$, 3.59 eV	$[V_O^{\bullet\bullet}] = 2[V_{Ce}^{////}] = 1.2 \times 10^{-6}$
Anti-Frenkel (eqn (2.2))	$K_{AF} = [O_i^{//}]\cdot[V_O^{\bullet\bullet}]$, 4.04 eV	$[O_i^{//}] = [V_O^{\bullet\bullet}] = 6.7 \times 10^{-11}$
Frenkel (eqn (2.5))	$K_F = [Ce_i^{\bullet\bullet\bullet\bullet}]\cdot[V_{Ce}^{////}]$, 7.36 eV	$[Ce_i^{\bullet\bullet\bullet\bullet}] = [V_{Ce}^{////}] = 2.8 \times 10^{-19}$

was also considered. As can be seen in Table 2, the formation of Frenkel defects requires a relatively high formation energy in comparison to the Schottky and Anti-Frenkel reactions. The equilibrium constants K of the corresponding defect formation reactions (2.1), (2.2) and (2.5) were also calculated for comparison purposes. Since statistical mechanics postulates that the fraction of defects follows the Boltzmann factor at equilibrium, then the equilibrium constant K was obtained as follows,

$$K = \exp(-E_{def}/k_B T) \quad (2.6)$$

where k_B and T are the Boltzmann constant and the absolute temperature, respectively. (Note that the Gibbs energy should be used instead of the defect formation energy to calculate the equilibrium constant.[37] However, we assumed the difference arising from the entropy (mainly due to vibrational one) and the volume change to be small enough for defect formation in solid state phases.) The results for the corresponding defect fractions are also listed in Table 2 and indicate quite small fractions of intrinsic defects in pure ceria.

Therefore, the main origin of oxygen vacancy creation can be ascribed to an extrinsic mechanism of doping CeO_2 with RE_2O_3 resulting in $Ce_{1x}RE_xO_{2-x/2}$. The formation of oxygen vacancies can be described as

$$RE_2O_2 \leftrightarrow 2RE_{Ce}^{\,/} + V_O^{\bullet\bullet} + 3O_O^X \quad (2.7)$$

On the other hand, another defect formation mechanism is also conceivable where an interstitial site is occupied by RE^{3+}.

$$2RE_2O_3 \leftrightarrow 3RE_{Ce}^{\,/} + RE_i^{\bullet\bullet\bullet} + 6O_O^X \quad (2.8)$$

In order to understand the defect chemistry on an atomistic level, we calculated the solution energy for Y_2O_3 doped CeO_2 as a typical representative. The computation was carried out assuming dilute conditions as mentioned before. Table 3 presents the calculated solution energies per Y_2O_3. The results indicate that the majority point defects compensating Y'_{Ce} are oxygen vacancies and not yttrium interstitials due to the much smaller solution energy of eqn (2.7) compared to eqn (2.8). Both obtained energies are positive, indicating that Y_2O_3 is

Table 3 Solution energies for the solution of Y_2O_3 in CeO_2 according to different solution reactions

Defect type (eqn. #)	Solution energy/ eV per Y_2O_3
Oxygen vacancy mechanism (eqn (2.7))	0.98
RE^{3+} interstitial mechanism (eqn (2.8))	2.61

not soluble in CeO_2 at low temperatures, while experimental studies clearly showed that RE_2O_3 and CeO_2 form a solid-solution up to a certain RE^{3+} concentration (see *e.g.* ref. 2). Similar results of positive solution energies were obtained for RE_2O_3 doped ZrO_2 using the classical potential model.[6] Probably, the solution Gibbs energy becomes negative by increasing the temperature due to the entropy effect and, in addition, the enthalpy may change with temperature (the synthesis is usually performed at temperatures above 1273 K). In addition, defect association, such as formation of Y^{3+}-oxygen vacancy pairs, decreases the solution energy as mentioned later. Thus, we regard oxygen vacancies (formed *via* eqn (2.1) for undoped ceria and *via* eqn (2.7) for RE_2O_3 doped ceria) as dominant conduction species.

Up to now, we discussed the defect formation mechanism from the viewpoint of infinitely diluted defects, *i.e.* we assumed that defects do not interact with each other. Now, we consider in addition two types of defect associates: (1) an associate of two oxygen vacancies, ($V_O^{\bullet\bullet}$–$V_O^{\bullet\bullet}$), and (2) an associate of an oxygen vacancy and a RE^{3+} dopant, ($RE_{Ce}^{/}$–$V_O^{\bullet\bullet}$). For the associate ($V_O^{\bullet\bullet}$–$V_O^{\bullet\bullet}$) we expect repulsive Coulombic interaction between the doubly charged oxygen vacancies, while we expect an atttractive Coulombic interaction for the associate ($RE_{Ce}^{/}$–$V_O^{\bullet\bullet}$) due to the opposite charges of the rare earth dopant and the oxygen vacancy. Both associates would cause a decrease of the oxygen ion conductivity due to a correlated motion of oxygen vacancies repelling each other and due to trapping of oxygen vacancies by RE^{3+}. In fact, defect association between an oxygen vacancy and a RE^{3+}-dopant was already found in fluorite-structured materials by means of atomistic simulations[5] and/or in experiments.[3] Thus, we evaluated the two defect association effects quantitatively by calculating the corresponding defect association energies ΔE_{V-V} and ΔE_{RE-V} as follows,

$$\begin{aligned}\Delta E_{V-V} &= [E_{tot}(V_O^{\bullet\bullet}\text{–}V_O^{\bullet\bullet})]-[2E_{tot}(V_O^{\bullet\bullet})] \\ &= [E_{tot}([Ce_{31}O_{62}]^{+}) + 32E_{tot}([CeO_2])] \\ &\quad -[2E_{tot}([Ce_{32}O_{63}]^{2+})] \end{aligned} \tag{2.9}$$

$$\begin{aligned}\Delta E_{RE-V} &= [E_{tot}\,(RE_{Ce}^{/}\text{–}V_O^{\bullet\bullet})] - [E_{tot}\,(RE_{Ce}^{/})] + E_{tot}\,(V_O^{\bullet\bullet})] \\ &= [E_{tot}\,([RECe_{31}O_{63}]^{+}) + 32E_{tot}([CeO_2])] \\ &\quad - [E_{tot}([RECe_{31}O_{64}]^{-}) + [E_{tot}([Ce_{32}O_{63}]^{2+})] \end{aligned} \tag{2.10}$$

where $E_{tot}(X)$ indicates the total energy of X. In both equations, the first and the second square-bracketed terms correspond to the total energies of associated defects and isolated defects, respectively. Note that a negative defect association energy ΔE_{RE-V} is often referred to as binding energy.

The calculated result for the defect association energy of two oxygen vacancies (eqn (2.9)) is $\Delta E_{V-V} \sim +0.77$ eV, *i.e.* the formation of two isolated oxygen vacancies is energetically more stable than the formation of the oxygen vacancy pair, ($V_O^{\bullet\bullet}$–$V_O^{\bullet\bullet}$). Despite the large energy penalty for formation of ($V_O^{\bullet\bullet}$–$V_O^{\bullet\bullet}$), this defect association will become important when the conductivity is considered, because in the conductivity one needs to consider at least the oxygen vacancy distribution in

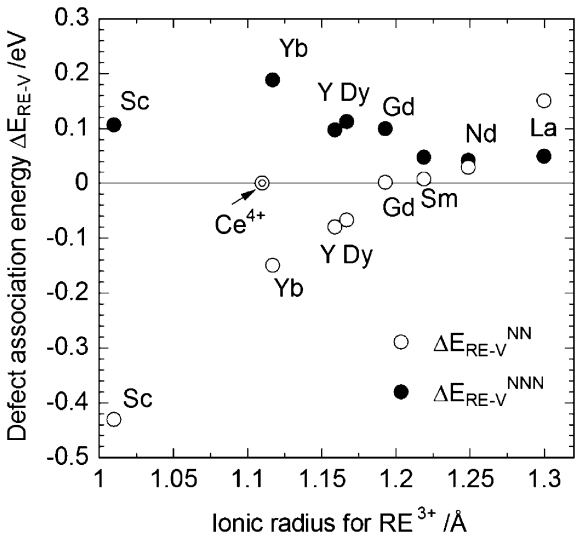

Fig. 1 Calculated defect association energies ΔE_{RE-V}^{NN} and ΔE_{RE-V}^{NNN} between a RE^{3+} dopant and an oxygen vacancy located on NN and NNN sites.

NNN sites (12 sites in CeO_2) that affects oxygen vacancy jumps to NN sites (6 sites in CeO_2).

The defect association energies of a RE^{3+}-dopant and an oxygen vacancy on nearest neighbour sites, ΔE_{Re-V}^{NN} and next-nearest neighbour sites, ΔE_{RE-V}^{NNN}, are plotted in Fig. 1 as a function of the ionic radii using eqn (2.10). (The ionic radii of RE^{3+} ions are referred to in Shannon's report.[38]). The NN association energy increases in a linear manner with the ionic radius of the dopants from −0.45 eV to +0.15 eV, whereas the NNN association energy is always positive and decreases slightly from ~0.05 to ~ 0.20 eV.[39] For NN interaction, the sign of the defect association energy changes from negative to positive by introducing RE^{3+}-dopants with ionic radii larger than ~1.2 Å (or larger than Gd^{3+}).. In other words, dopants with smaller ionic radii than Gd^{3+} trap an oxygen vacancy at the NN site, while larger dopants repel it. The defect association energy is a strong function of the ionic size of the dopant RE^{3+}, showing that structural distortions around defects contribute to stabilization or destabilization of defect association. It is noted that the ionic radius corresponding to $\Delta E_{RE-V}^{NN} = 0$ differs from the ionic radius of Ce^{4+} (the ionic radius of Ce^{4+} is ~ 1.11 Å[38]). This indicates that local structural modifications induced by dopants of different size compared to the host Ce^{4+} ions would not be the only factor to account for the defect association energy. One of the possible reasons is the difference of the valence states of RE^{3+} and Ce^{4+}.

To further investigate defect association between a RE^{3+} dopant and an oxygen vacancy, the variation of the defect association energy as a function of the coordination number (CN) of a vacancy with RE^{3+} (RE = Sc, Y, La) ions was calculated and is plotted in Fig. 2. In this figure, an isolated oxygen vacancy that is surrounded by a single or plural NN RE^{3+} ions is considered (CN = 0 corresponds to an oxygen vacancy in pure Ceria). The hatched lines in Fig. 2 indicate the linear extrapolation of the defect association energies for CN = 0 and CN = 1. Hence, these hatched lines correspond

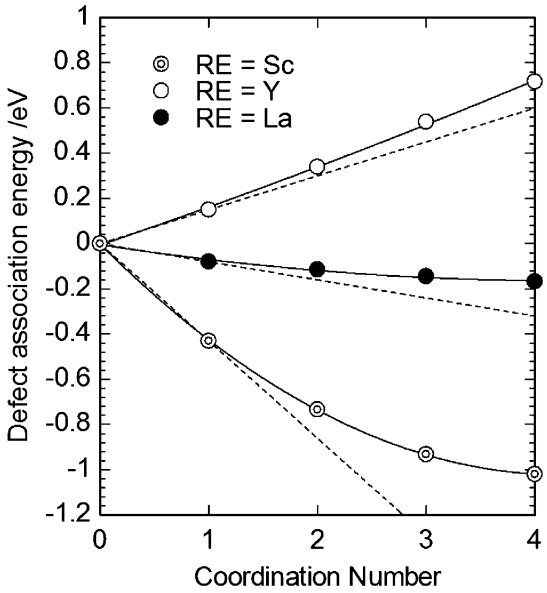

Fig. 2 Variation of the defect association energy ΔE^{NN}_{RE-V} between an oxygen vacancy and RE^{3+} dopants as a function of the number of RE^{3+} dopants coordinating the oxygen vacancy. (RE = Sc, Y, La).

to the simple assumption that the defect association energy consists only of pair-interactions between an oxygen vacancy and RE^{3+} dopants. In all cases, the defect association energy for plural coordination with RE^{3+} is above the extrapolated, hatched line in Fig. 2, probably due to dopant–dopant repulsion. The dependence of the defect association energy on the CN is nonlinear, especially obvious in the case of Sc^{3+} doping. However in all cases the defect association energy varies monotonously with the CN of RE^{3+} ions, so that the tendency shown in Fig. 1 remains the same: doping with smaller ions stabilizes an oxygen vacancy on NN sites, while doping with larger ions destabilizes it.

To sum up the defect chemistry of RE_2O_3 doped CeO_2, our calculations have shown the following results:

—RE^{3+} substitution for Ce^{4+} leads preferentially to the formation of oxygen vacancies,

—RE^{3+} dopants smaller than Gd^{3+} tend to trap the oxygen vacancy at the NN site strongly, while RE^{3+} dopants larger than Gd^{3+} repel the oxygen vacancy from NN sites.

4. Results: oxygen ion migration

4.1 Pure CeO_2

Fig. 3 shows three conceivable migration pathways (Paths 1–3) for oxide ions between adjacent tetrahedral sites in CeO_2, corresponding to an opposite oxygen vacancy hopping along the ⟨100⟩, ⟨110⟩ and ⟨111⟩ direction, respectively. If one considers straightforward hopping, Path 1 requires passing through a dumbbell of two cerium ions in the middle of two adjacent tetrahedral oxygen sites. In this case, the minimum interatomic distance between the hopping oxide ion and the cerium ions is ~1.95 Å. Therefore, strong Coulombic attraction and large steric repulsion is expected for Path 1. For Path 3, the oxide ion hops *via* a large interstitial space (4b site) which is coordinated by eight oxide ions with a

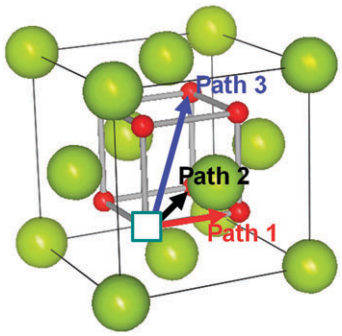

Fig. 3 Three possible oxide ion migration pathways (Path 1–3) in the fluorite structure of ceria. Large light green spheres indicate cerium, the white square indicates an oxygen vacancy and small red spheres correspond to oxide ions.

distance of ~ 2.38 Å, so that local electrostatic repulsion by surrounding anions may prevent the oxide ion from hopping along Path 3. Path 2 may be a moderate situation with a smaller CN of oxygen ions and a larger distance from cations except for one closest Ce^{4+}.

Fig. 4 presents the computational results of the energy profiles (a) and the corresponding trajectories (b)–(d) for the above three types of jumps obtained by the NEB approach. Note that the horizontal axis in Fig. 4a refers to the jumping 'oxygen vacancy', and the projected migration distance indicates its position projected onto the straight line connecting the initial (refers to 0) and final (refers to 1) oxygen vacancy positions. All the energy profiles show a maximum at the middle between the initial and final positions. Obviously, the activation energies of Paths 2 and 3 are much larger than that of Path 1 (~0.5 eV), so that a negligible contribution to the oxygen ionic conductivity is expected for Paths 2 and 3. The oxide ion jumps straightforward for Paths 1 and 3, while

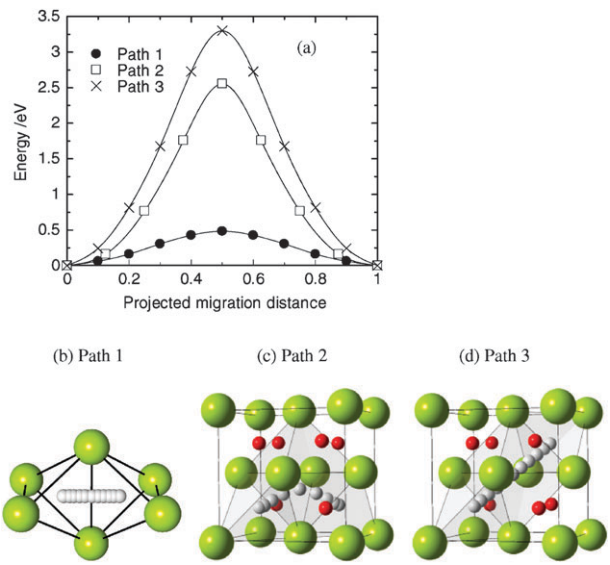

Fig. 4 (a) Energy profiles during oxide ion hopping for Paths 1–3, and (b)–(d) corresponding trajectories of hopping oxide ions. In (b)–(d), large light-green spheres indicate cerium and small white and red (brighter and darker small) spheres correspond to hopping and non-hopping oxide ions, respectively.

Path 2 shows a curved trajectory passing through the vicinity of interstitial sites being close to the transition point of Path 3. As a result, the activation energies of paths 2 and 3 are both relatively large.

Referring to a previous report by Wang *et al.*,[40] the migration enthalpy for pure CeO_2 would be around 0.6 eV. Fabor *et al.* also reported the migration enthalpy of doped ceria to be 0.5 eV using NMR techniques.[41] Thus, the present computational results for Path 1 show quantitative accordance with the experimental results, supporting the validity of the present results. Moreover, the present computational results regarding the trajectories of oxide ion migration agree in essence with the results of previous studies. For example, Shimojo *et al.* used molecular dynamics simulations[9] and showed for yttria-doped ZrO_2 with fluorite structure that oxide ions hop dominantly along the ⟨100⟩ direction between adjacent tetrahedra formed by the cations (Path 1). More recently, Yashima *et al.* investigated the oxygen migration path in Y_2O_3 doped CeO_2 using neutron powder diffraction combined with the maximum entropy method.[42] Their results indicate that the oxide ion migrates mainly along the ⟨100⟩ direction, in agreement with the results of the present computation (Path 1). However, the experimentally observed migration path is not a straight line as depicted in Fig. 4b, but a curved line. In addition, their results also indicate oxygen ion migration along the ⟨110⟩ direction (Path 2 in this paper). We believe, however, that the curved pathway for Path 1 and the observed oxide ion migration along Path 2 may be related to the very high temperature of 1434 °C in these experiments. As we are interested in oxygen ion conduction at much lower temperatures we will neglect, hereinafter in this paper, the contribution of conduction pathways 2 and 3 due to their much larger activation energies for oxygen ion jumps.

4.2 RE_2O_3-doped CeO_2

In this section, the effect of RE^{3+}-doping on the oxide ion jumps is investigated. We assume that only RE^{3+}-ions on nearest neighbour positions (NN-RE^{3+}) affect the oxide ion hopping, since in section 3.2 it was found that defect association between a RE^{3+}-dopant and an oxygen vacancy is especially significant if both occupy NN positions. However, even with this constraint there are numerous configurational degrees of freedom, which makes it difficult to perform computations by first-principles DFT for all conceivable arrangements of oxygen vacancies and dopants. Thus, from now on we consider dopant–vacancy interactions only within the two adjacent tetrahedra that are defined by Path 1 (see Fig. 4(b)). In this case, the energy profile during the jump of an oxide ion from one specific site to an adjacent specific site depends only on the cation configuration in the two adjacent tetrahedra (see Fig. 5a). Before the jump, the oxide ions resides in a tetrahedral site, and there are five possible cation configurations depending on the coordination number of RE ions; namely $O_{Ce,Ce,Ce,Ce}$, $O_{Ce,Ce,Ce,RE}$, $O_{Ce,Ce,RE,RE}$, $O_{Ce,RE,RE,RE}$, and $O_{RE,RE,RE,RE}$. During the jump from one tetrahedron to another, the oxygen ion has to cross their common edge that could be a Ce–Ce, a Ce–RE, or a RE–RE edge. After the jump, there are again five possible cation configurations in the second tetrahedron. As the two tetrahedra share a common edge, there are only 30 distinguishable types of oxide ion jumps.[9] Due to the limitations of computational resources, we chose five important hopping models (Model A–E shown in Fig. 5) for the following reasons. (Note that Model A is exactly the same as considered previously for Path 1 in Fig. 3.) Models A, B and C differ by the number of dopants in the shared edge that has to be crossed by the jumping oxygen ion (Ce–Ce, Ce–RE, RE–RE). However, in all three models the configuration of the oxygen vacancy and the RE^{3+}-dopants before and after the jump remains unchanged, which means that in these symmetric cases the corresponding association energies remain unchanged. On the other hand, models D and E reflect the asymmetric effect of defect association, since the coordination number of RE-dopants with oxide ions is different before and after the jump. In model D one "bond" between the oxygen vacancy and the RE^{3+}-dopant is broken, in model E two "bonds" are broken.

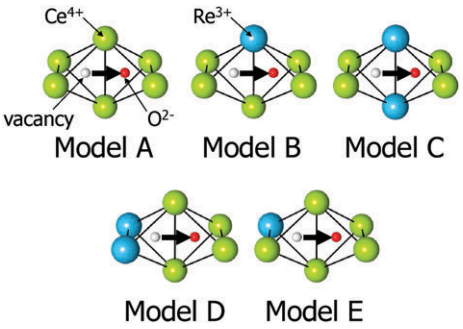

Fig. 5 Five types of nearest neighbour (NN) cation configurations for oxygen vacancy hopping models examined in this study in RE^{3+} substituted ceria. The smaller red and white (darker and brighter small) spheres represent an oxide ion and a vacancy, and the larger light green and light blue (brighter and darker large) spheres indicate Ce^{4+} and RE^{3+}, respectively. Note that the projected migration distance refers to the oxygen vacancy position.

At first, yttrium was chosen as typical trivalent dopant. The above 5 jump models were evaluated and the results are shown in Fig. 6. The energy profiles corresponding to oxide ion jumps for models A–C (Fig. 6a) exhibit the maximum at the middle between the two adjacent tetrahedral sites as in the case of pure CeO_2 in Fig. 3. Obviously, the Y^{3+} occupation at the

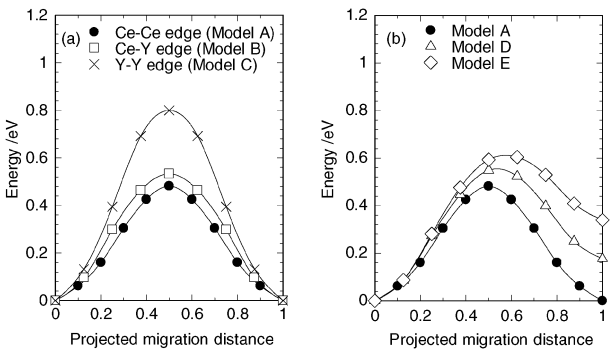

Fig. 6 Energy profiles for Models A–E (see Fig. 5) in yttria doped ceria. Note that the projected migration distance refers to the 'oxygen vacancy' position.

shared-edge sites causes an increase in the activation energy. This increase is no linear function of the number of Y^{3+} ions: a single Y-ion in the edge increases the migration energy by 0.05 eV (model B) while two Y-ions cause an increase of 0.30 eV (model C). As is the case of Models B and C, Models D and E show a change in the activation energy due to the Y occupation in the first tetrahedron (Fig. 6b). However, the obtained energy profiles are asymmetric, demonstrating that the oxygen vacancy prefers to be located on a NN-position of the Y^{3+}-dopant (*vice versa* for the oxide ion). Note that the energy differences between the two oxygen sites correspond to the difference of the defect association energies between an oxygen vacancy and one (or two) Y^{3+}-ion(s) on NN- and on NNN-sites (see also Fig. 1). The increase of the activation energy is almost linear against the number of Y^{3+}-ions as can be seen in Fig. 6. This can be ascribed to the fact that the defect association energy showed an almost linear behaviour as a function of the number of NN Y^{3+}-ions (see Fig. 2 for CN $\leq$ 2 and RE = Y). Thus, there seems to be a simple relationship between the defect association energy and the activation energy for oxygen ion jumps. Here, we propose a simple model where the activation energy E_A for oxide ion jumps between two adjacent tetrahedra with different cation configurations can be decomposed into two contributions, $E_A = \Delta E_{\mathrm{edge}} - (N_{\mathrm{RE}}^{\mathrm{NN}}\,\Delta E_{RE\text{–}V}^{\mathrm{NN}} + N_{\mathrm{RE}}^{\mathrm{NNN}}\,\Delta E_{RE\text{–}V}^{\mathrm{NNN}})$. Here ΔE_{edge} depends only on the cation pair forming the shared-edge of the two adjacent tetrahedra and corresponds to the activation energies of models A, B and C (see Fig. 6(a)). N_{RE} is the CN of the oxygen vacancy with RE (except for RE at shared-edge sites), and $\Delta E_{\mathrm{RE\text{–}V}}$ indicates the defect association energy as mentioned above. Using this simple equation, one can obtain the activation energies for forward and backward oxide ion jumps for arbitrary configurations of Ce^{4+}- and RE^{3+}-cations only by calculating Models A–C and the defect association energies $\Delta E_{RE\text{–}V}^{\mathrm{NN}}$ and $\Delta E_{RE\text{–}V}^{\mathrm{NNN}}$. Table 4 compares the activation energies for forward and backward jumps predicted by the above method with the exact results from the first-principles study. The predicted activation energies show good accordance with the first-principles results (energy difference is less than 40 meV). This prediction method for the jump activation energy would be beneficial for calculating the macroscopic ionic conduction behaviour. To demonstrate, we calculated the conductivity behaviour using a model that was proposed in a previous report.[16] This model considers the oxygen vacancy distribution using mass action equations and jump frequencies using activation energies for the considered configurations of tetrahedra. However, this model[16] considers only NN interactions and assumes a constant attempt frequency (related to the vibrational properties) for oxygen vacancy jumps which is independent of the local cation configuration and temperature. Therefore, the simulated ionic conductivities are compared only on a relative scale. Fig. 7 shows the predicted ionic conductivity behaviour at 200 and 600 °C as a function of composition x in $Y_xCe_{1-x}O_{2-x/2}$. The optimized composition, x_{opt}, for ionic conductivity is located around $x \sim 0.16$ and 0.28 at 200 and 600 °C, respectively. Both predicted results overestimate the optimized compositions against experimental results ($x_{\mathrm{opt}} \sim 0.08$ and ~ 0.12 at 455 and 833 K, respectively[43]). However, the present predictions capture two important features, (i) the existence of optimized compositions, and (ii) these optimized compositions shift to larger values by increasing the temperature. The deviation between predicted and experimental values may arise from disregarding both the NNN site contribution and the repulsive vacancy–vacancy interactions in the conductivity model.[16] Similarly, the present predictions also showed increase of the averaged activation energies with the composition x, showing qualitative accordance with experimental results at $x > \sim 0.04$.[41] We will modify the model and discuss it comprehensively in the near future.[44]

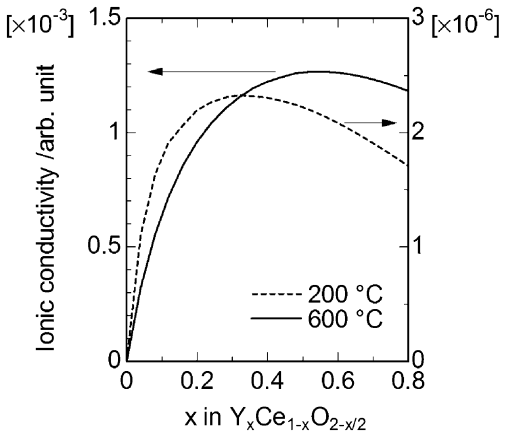

Fig. 7 Calculated ionic conductivity of $Y_xCe_{1-x}O_{2-x/2}$ as a function of composition x. The results were obtained using the conductivity model reported in ref. 30 and taking the activation energies calculated in this study.

Table 4 Activation energies for oxygen vacancy jumps between adjacent tetrahedral sites in Y-doped ceria. Forward jump indicates an oxygen vacancy jump from left to right in Fig. 5, and backward jump indicates the reverse jump

Jump type	Activation energy/eV (First-principles DFT and NEB)		Activation energy/eV (Prediction according to main text)	
	Forward jump	Backward jump	Forward jump	Backward jump
Model A	0.482		N/A	N/A
Model B	0.533		N/A	N/A
Model C	0.800		N/A	N/A
Model D	0.549	0.372	0.563	0.386
Model E	0.604	0.264	0.643	0.289

In addition, the above scheme would apply to various RE^{3+} dopants as well as Y^{3+} doping. However, we note that smaller RE^{3+} dopants (such as Sc^{3+}) show a nonlinear dependence of the defect association energies on the CN (see Fig. 2), so that linear extrapolation from Model D to Model E is not appropriate.

Finally we consider in Fig. 8 the obtained energy barrier ΔE_{edge} (or the jump activation energies of Models B and C) for various RE dopants as a function of their ionic radii.[38] The energy barrier for pure CeO_2 (Model A) is also plotted for comparison purpose. ΔE_{edge} increases with the ionic radius of RE^{3+} and is larger for Model C (RE–RE edge) than for Model B (RE–Ce edge) for all RE–dopants, except for Sc where both

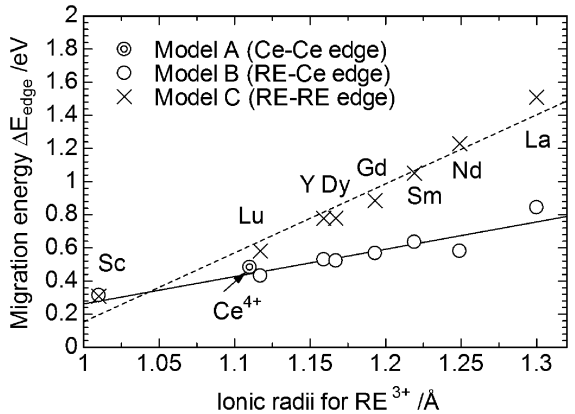

Fig. 8 Calculated migration energies ΔE_{edge} for oxygen ion jumps in Models A, B and C for RE_2O_3 doped CeO_2 as a function of the ionic radii.

values are about the same.[39] The slope for Model C is steeper than that for Model B. The above tendency shows good accordance with first-principles DFT studies by Andersson *et al.*,[11] especially for Model C (RE–RE edge) due to the consistence of the structural models in both computations. On the other hand, it is difficult to compare their results directly with Model A (Ce–Ce edge) and Model B (Ce–RE edge), since they calculated the migration barrier energies using one specific Ce/RE/O/vacancy configuration, which essentially contains NN and NNN defect association energies and asymmetric effects as mentioned before.

We infer that the larger activation energy in Model C may be ascribed to the Coulombic interactions, since smaller attractive interactions are expected at the transition state of Model C (RE^{3+}–O^{2-}–RE^{3+}) than for Model B (Ce^{4+}–O^{2-}–RE^{3+}). In this respect, the larger migration barrier for doping with larger RE^{3+} ions could also be explained by the smaller Coulombic interaction because of the larger interatomic distance between the dopant and the oxygen vacancy. Accordingly, the present results show that improvement of the oxide ionic conductivity can be achieved by using smaller RE^{3+} doping in terms of the migration barrier ΔE_{edge}. On the other hand, smaller dopants cause strong binding of the vacancy. Further investigations are needed to reveal the original reasons for the tendency shown in Fig. 8.

5. Summary

Atomistic level studies on defect chemistry and oxygen migration in Re_2O_3 doped CeO_2 have been conducted using first-principles DFT. The results show that the dominant point defects are oxygen vacancies charge compensating the aliovalent RE^{3+} dopants. Oxide ion (or oxygen vacancy) hops occur straightforward along the ⟨001⟩ directions connecting two NN oxygen sites. Defect association effects are non-negligible between RE^{3+} ions and oxygen vacancies. The obtained defect association energies show that smaller RE^{3+} ions strongly trap oxygen vacancies, while larger RE^{3+} ions repel them. Moreover, the energy barrier for oxide ion hopping is a strong function of the ionic radius of the RE^{3+} ions which are located at the shared edge of two adjacent tetrahedra. Increase of RE^{3+} ions causes a reduction of the hopping energy barrier, and *vice versa*. Hence, the following trade-off relationship is found; (1) the reduction of the energy barrier by doping with smaller RE^{3+} would be accompanied by trapping of an oxygen vacancy at the NN sites of the dopant, whereas (2) doping with larger RE^{3+} decreases the trapping effect of oxygen vacancies but increases the energy barrier. Thus—depending on the relative magnitude of the effects—both an increase and a decrease of ionic conductivity are possible. (In the latter situation, larger RE^{3+} ions prevent defect association, so that the reduction of the conductivity may be due to the decrease of the effective volume for conduction space.) Such a relationship may account for the previous experimental results that the ionic conductivity showed a maximum for the dopants with intermediate ionic radii.[3,4] Our results were obtained from 5 specific local models for oxygen vacancy jumps where only NN cation arrangements were considered (see Fig. 5). We believe, however, that the DFT energies based on these limited configurations can be extended to approximate the energies for more complex configurations, following the same strategy that was used to get the results in Table 4. Then it should be possible to consider also extreme situations such as (1) a random distribution of dopants and (2) an ordered distribution of dopants. Finally, to understand further why the defect association energy and migration energy strongly depend on the ionic radii of the dopant ions, we will discuss the local structural modifications around defects and in the transition states of hopping ions in the near future.

Acknowledgements

This work was supported partly by Grant-in-Aid for Scientific Research (No. 20760450) from Ministry of Education, Culture, Sports, Science and Technology (Japan). Fig. 3 and 4 were drown with VESTA developed by K. Momma and F. Izumi.[46]

References

1 T. H. Etsell and S. N. Flengas, *Chem. Rev.*, 1970, **70**, 339.
2 H. Inaba and H. Tagawa, *Solid State Ionics*, 1996, **83**, 1.
3 R. Gerhardt-Anderson and A. S. Nowick, *Solid State Ionics*, 1981, **5**, 547.
4 K. Eguchi, T. Setoguchi, T. Inoue and H. Arai, *Solid State Ionics*, 1992, **52**, 165.
5 V. Bulter, C. R. A. Catlow, B. E. F. Fender and J. H. Harding, *Solid State Ionics*, 1983, **8**, 109.
6 M. O. Zacate, L. Minervini, D. J. Bradfield, R. W. Grimes and K. E. Sickafus, *Solid State Ionics*, 2000, **128**, 243.
7 X. Wei, W. Pan, L. Cheng and B. Li, *Solid State Ionics*, 2009, **180**, 13.
8 H. Yoshida, H. Deguchi, K. Miura, M. Horiuchi and T. Inagaki, *Solid State Ionics*, 2001, **140**, 191.
9 F. Shimojo and H. Okazaki, *J. Phys. Soc. Jpn.*, 1992, **61**, 4106.
10 H. Yoshida, T. Inagaki, K. Miura, M. Inaba and Z. Ogumi, *Solid State Ionics*, 2003, **160**, 109.
11 D. A. Andersson, S. I. Simak, N. V. Skorodumova, I. A. Abrikosov and B. Johansson, *Proc. Natl. Acad. Sci. U. S. A.*, 2006, **103**, 3518.
12 A. D. Murray, G. E. Murch and C. R. A. Catlow, *Solid State Ionics*, 1986, **18–19**, 196.
13 R. Krishnamurthy, Y.-G. Yoon, D. J. Srolovitz and R. Car, *J. Am. Ceram. Soc.*, 2004, **87**, 1821.
14 R. Krishnamurthy, D. J. Srolovitz, K. N. Kudin and R. Car, *J. Am. Ceram. Soc.*, 2005, **88**, 2143.

15 R. Pomprasertsuk, P. Ramanarayanan, C. B. Musgrave and F. B. Prinz, *J. Appl. Phys.*, 2005, **98**, 103513.
16 M. Martin, *J. Electroceram.*, 2006, **17**, 765.
17 G. Kresse and J. Furthmuller, *Phys. Rev. B*, 1996, **54**, 11169.
18 G. Kresse and J. Furthmuller, *Comput. Mater. Sci.*, 1996, **6**, 15.
19 J. P. Perdew, K. Burke and M. Ernzerhof, *Phys. Rev. Lett.*, 1996, **77**, 3865.
20 P. E. Blöchl, *Phys. Rev. B*, 1994, **50**, 17953.
21 V. I. Anisimov, J. Zaanen and O. K. Andersen, *Phys. Rev. B*, 1991, **44**, 943.
22 V. I. Anisimov, J. Zaanen and O. K. Andersen, *Phys. Rev. B*, 1993, **48**, 16929.
23 A. I. Liechtenstein, V. I. Anisimov and J. Zaanen, *Phys. Rev. B*, 1995, **52**, R5467.
24 M. Nolan, S. Grigoleit, D. C. Sayle, S. C. Parker and G. W. Watson, *Surf. Sci.*, 2005, **576**, 217.
25 M. Nolan, J. E. Fearon and G. W. Watson, *Solid State Ionics*, 2006, **177**, 3069.
26 J. L. F. Da Silva, M. V. Ganduglia-Pirovano, J. Sauer, V. Bayer and G. Kresse, *Phys. Rev. B*, 2007, **75**, 089901.
27 J. C. Conesa, *Catal. Today*, DOI: 10.1016/j.cattod.2008.11.005.
28 H. Jonsson, G. Mills and K. M. Jacobsen, in *Classical and Quantum Dynamics in Condensed Phase Simulations*, ed. B. J. Berne, G. Ciccotti and D. F. Coker, World Scientific, Singapore, 1998.
29 F. D. Murnaghan, *Proc. Natl. Acad. Sci. U. S. A.*, 1944, **30**, 244.
30 Z. Yang and T. K. Woo, *J. Chem. Phys.*, 2004, **120**, 22.
31 N. V. Skorodumova, M. Baudin and H. Kermansson, *Phys. Rev. B*, 2004, **69**, 075401.
32 N. V. Skorodumova, R. Ahuja, S. I. Simak, I. A. Abrikosov, B. Johansson and B. I. Lundqvist, *Phys. Rev. B*, 2001, **64**, 115108.
33 G. Liu, J. A. Rodriguez, J. Hrbek, J. Dvorak and C. H. F. Peden, *J. Phys. Chem. B*, 2001, **105**, 7762.
34 L. Eyring, *Handbook on the Physics and Chemistry of Rare Earths*, ed. K. A. Gschneider and L. Eyring, North-Holland, Amsterdam, 1979.
35 L. Gerward and A. S. Staun-Olsen, *Powder Diffr.*, 1993, **8**, 127.
36 A. Nakajima, A. Yoshihara and M. Ishigame, *Phys. Rev. B*, 1994, **50**, 13297.
37 For example, A. F. Kohan, G. Ceder, D. Morgan and C. G. Van de Walle, *Phys. Rev. B*, 2000, **61**, 15019.
38 R. D. Shannon, *Acta Crystallogr., Sect. A*, 1976, **32**, 751.
39 The fact that the DFT energies without the DFT + U technique show a systematic dependence on the ionic radii (see Fig. 1 and 8) may ensure the present computational quality even for the compounds that contain localized 4f electrons. (Note that Ce^{4+}, Sc^{3+}, Y^{3+} and La^{3+} do not possess 4f electrons, while the other RE^{3+} ions possess 4f electrons).
40 D. Y. Wang, D. S. Park, J. Griffith and A. S. Nowick, *Solid State Ionics*, 1981, **2**, 95.
41 J. Fabor, C. Geoffroy, A. Roux, A. Sylvestre and P. Abelard, *Appl. Phys.*, 1989, **A49**, 225.
42 M. Yashima, S. Kobayashi and T. Yasui, *Faraday Discuss.*, 2007, **134**, 369.
43 A. S. Nowick, in *Diffusion in Crystalline Solids*, ed. G. E. Murch and A. S. Nowick, Academic, New York, 1984, ch. 3.
44 Another factor that affects the dopant concentration for maximum ionic conductivity would be the correlation of successive oxygen vacancy jumps which is due to the fact that the jump probability depends on the local cation configuration and vacancy-vacancy exchanges are forbidden. These effects are summarized in the so-called physical correlation factor for diffusion (see ref. 45). The present model[16] considers only NN correlation effects. Nevertheless, inclusion of the NN correlation effects improved significantly the estimation of diffusion coefficients according to the literature[13]).
45 A. D. Le Claire, *Correlation Effects in Diffusion in Solids; Physical Chemistry: An Advanced Treatise*, ed. W. Jost, Academic Press, New York, 1970, vol. X, pp. 261.
46 K. Momma and F. Izumi, *J. Appl. Crystallogr.*, 2008, **41**, 653–658.